A two-photon lensless endoscope with a double-clad tapered multi-core fiber

Luca Genchi, Matthias Hofer, Adrien Carron, Fatima El Moussawi, Aymeric Pastre, Rémy Bernard, Damien Labat, Andy Cassez, Rosa Cossart, Olivier Vanvincq, et al.

To be published in Optics Letters:

Title: A two photon lensless endoscope with a double-clad tapered multi-core fiber

Authors: Luca Genchi,Matthias Hofer,Adrien Carron,Fatima El Moussawi,aymeric pastre,Remy Bernand,Damien LABAT,Andy Cassez,Rosa Cossart,Olivier Vanvincq,Geraud Bouwmans,Siddharth Sivankutty,Herve Rigneault,Esben Andresen

Accepted: 11 February 25

Posted 12 February 25

DOI: https://doi.org/10.1364/OL.550709

A two photon lensless endoscope with a double-clad tapered multi-core fiber

LUCA GENCHI[1,†], MATTHIAS HOFER[1,†], ADRIEN CARRON[2], FATIMA EL MOUSSAWI[2], AYMERIC PASTRE[2], RÉMY BERNARD[2], DAMIEN LABAT[2], ANDY CASSEZ[2], ROSA COSSART[3], OLIVIER VANVINCQ[2], GÉRAUD BOUWMANS[2], SIDDHARTH SIVANKUTTY[2], HERVÉ RIGNEAULT[1], AND ESBEN RAVN ANDRESEN[2,*]

[1] *Aix-Marseille Univ., CNRS, Centrale Med, Institut Fresnel, Marseille, France.*
[2] *Univ. Lille, CNRS, UMR 8523 PhLAM-Physique des Lasers, Atomes et Molécules, F-59000 Lille, France.*
[3] *INSERM, Aix-Marseille Univ., CNRS, INMED, Marseille, France.*
[†] *These authors contributed equally to this work.*
[*] *esben.andresen@univ-lille.fr*

Compiled February 10, 2025

We present a novel multi-core fiber-based lensless micro-endoscope incorporating several key innovations: a Fermat's golden spiral core layout, a low-index polymer cladding, and a longitudinally varying fiber diameter. This fiber design enables efficient focusing of ultrashort pulses and collection of the fluorescence signal with both diffraction-limited resolution and field of view. These advancements address several long-standing challenges in the development of ultra miniaturized nonlinear endoscopes. We characterize the device's performance by evaluating the Strehl ratio, field of view, and memory effect. Finally, we demonstrate its application to biological cellular samples by performing two-photon excited fluorescence imaging in an endoscopic configuration.

http://dx.doi.org/10.1364/ao.XX.XXXXXX

The lens-less endoscope is a promising ultra-miniaturized imaging tool which may enable minimally invasive and high-resolution observation for example of neuronal activity in-vivo inside deep brain areas [1–3]. While reports of lensless endoscopes based upon multi-mode fiber are predominant [1–5], reports of lensless endoscopes based upon multi-core fiber (MCF) are also numerous [6–11].

The significance of multi-core fibers (MCFs) as a key enabling technology for lensless endoscopes employing nonlinear contrast mechanisms has been discussed in Ref. [12] and Ref. [13]. In short, the two major advantages that an MCF brings are the minimal temporal distortions to a ultrafast laser pulse [14, 15] and a very high robustness to bending [9, 16]. Both these advantages arise due to the highly homogeneous individual cores which exhibit very little cross-talk [12]. This low cross-talk is ensured by the sparse distribution of the cores over the transverse face of the MCF.

In a lensless endoscope, the fiber emits a number of mode fields, and one typically aims to coherently superpose these modes to focus on a grid of transverse positions by means of wave front shaping. So, while the sparsity ensures low cross-talk which in turn has the advantageous consequence of memory effect allowing for fast point-scanning [17, 18], an adverse effect is a generally poor intensity in the focal spot ie the point-spread function (PSF), containing typically only 2-3 % of the total energy [8, 13, 19].

In Ref. [13] we explored longitudinal tailoring of the MCF diameter through tapering and showed that suitably tapering the distal end of the MCF allows improvement in PSF intensity and, consequently, two-photon fluorescent signal yield. We highlighted that for suitable choices of taper profile, these improvements are not accompanied by significant adverse effects like higher cross-talk or robustness to conformational changes. The idea of conferring improved performance or new functionalities on an instrument using tapered optical fiber has also been reported in neighboring domains such as photo-acoustic endoscopy [20] and fiber-optic depth-resolved fluorescence lifetime photometry [21].

In this letter we report an implementation of a multi-core fiber-based lensless micro-endoscope which integrates the following new elements as compared to Ref. [13]. A MCF with cores laid out on a Fermat's golden spiral pattern which assures a marked amelioration in the shape of the point-spread function, particularly in two-photon imaging. The tailoring of the longitudinal profile of the MCF, with conically down-tapered segments at both ends which results in a significant increase in the intensity of the point-spread function and, consequently, two-photon fluorescence signal yield. The application of a low-index polymer coating on the tapered MCF which enables efficient collection of epi-scattered fluorescence through a large numerical aperture of 0.48. We perform a characterization of the reported implementation in terms of several performance metrics and as a demonstration, we demonstrate two-photon imaging of biological samples—fixed ATTO-488-labeled mammalian osteosarcoma cells and GFP-labeled neurons in brain slices—with high efficiency proximal detection of the fluorescence signal and operating at the diffraction limit imposed by the MCF optogeometric parameters.

The MCF realized for this study was designed with parabolic-index cores having V-parameter equal to 5.0, guiding two modes. This design choice minimizes the inter-core group delay dispersion cf Ref. [13] and Ref. [22] and so minimizes the group delay spread between fs-pulses propagating on the fundamental mode in different cores. As for core layout we chose a Fermat's golden spiral layout, ie where position of the n'th core is defined by, in cylindrical coordinates, $\rho_n = \Lambda\sqrt{n}$ with Λ is a scaling parameter proportional to the average distance between cores ; and $\theta_n = n\pi(3-\sqrt{5})$. To fabricate the MCF, first a total of 120 holes of 230 mm depth and 2.1 mm diameter were drilled into a 50 mm diameter silica rod on a Fermat's golden spiral layout. Germanium doped glass rod with parabolic index profile and index step Δn = $30{\cdot}10^{-3}$ were inserted into these holes. This preform was drawn to fiber at the FiberTech Lille technology Platform, University of Lille, France. The obtained parameters were : Outer diameter 250 μm; core diameter 5 μm; Λ = 10.5 μm. We employ a glass processing station (LZM-100, Fujikura) to obtain conically-tapered sections at both the proximal and distal end of a 30 cm long segment of the MCF. Figure 1(a) depicts the geometry of the MCFs having undergone this post-processing. Representative examples of the point-spread functions from both a periodic, triangular core layout , and the current, aperiodic Fermat's golden spiral core layout [Figs. 1(b) and 1(c)] are presented in Figs.1(d) and 1(e) and showcase the desired amelioration, suppression of the secondary lobes, brought about by the new layout. Three MCF samples were produced, labeled "Fiber O", "Fiber A" and "Fiber B". All samples have a proximal segment with diameter reduced to 0.6 times the original diameter, reducing locally the V parameter to <3.5 and assuring that injected light is coupled only into the fundamental mode of the bi-mode cores. Both fibers have 25 mm long transition regions between the end segments and the middle segment assuring adiabaticity. The fibers differ in the diameter of the distal segments, in Fiber O unchanged, in Fiber A reduced to 0.6 times the original, in Fiber B reduced to 0.4 times the original. The double tapered MCFs were re-coated by successive multi-layer deposition using a home made device [23, 24]. Low refractive index polymer (Desolite DF-0016, n = 1.37) with a thickness of 45 µm was first deposited and UV-cured, then high index polymer (Desolite DF-2042) was deposited and UV-cured with a thickness about 60 µm. In this configuration, the entire innermost cladding of the MCF is functionally the core of a large core step-index multi-mode fiber with an index difference of about $80{\cdot}10^{-3}$ to the the low-index polymer cladding, resulting in a collection NA = 0.48.

The experimental setup used to perform the characterization of the focusing efficiency through the double-clad multi-core fiber and the subsequent two-photon imaging experiments is sketched in Fig. 2 and is described below: A femtosecond laser (λ = 920 nm and t_{pulse} = 180 fs) is expanded and reflected off a liquid-crystal based spatial light modulator (SLM, X10468, Hamamatsu). A phase pattern is calculated analytically using a superposition of phase-only gratings and lenslet array such that it generates an array of focused beamlets whose relative spatial arrangement corresponds to the arrangement of the cores of the multi-core fiber. This focused array is then relayed by a series of telescopes with an effective demagnification (M $\approx$ 80) such that it matches the mode-field diameter of the individual cores of the MCF. This 1 : 1 mapping of pixel groups (about 40×40 pixels) on the SLM to the cores of the fiber enables fine control over the relative positions, coupling angles and divergence. Furthermore, the relative phases between the beamlets can also be tuned by applying phase-offsets between their corresponding pixel groups.

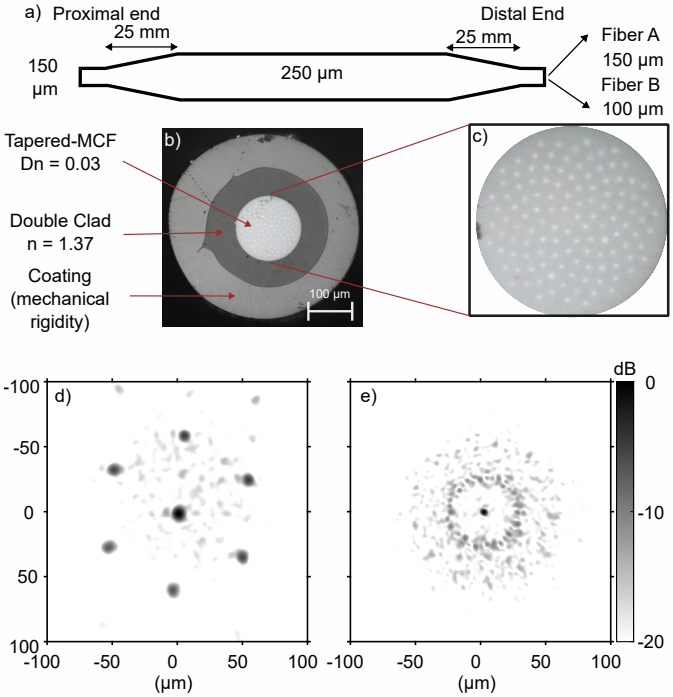

Fig. 1. (a) The longitudinal profile of the the MCF samples after tapering. Left is the proximal side (closest to the laser), right is the distal side (closest to the sample). (b) Example image of an end face of Fiber A showing the resulting MCF recoated with a first low-index and a second high-index polymer. (c) Enlarged wiew of the MCF end face. (d) Example point-spread function for a periodic core layout. (e) Example point-spread function with the current, aperiodic Fermat's golden spiral core layout.

After an initial coarse alignment of the MCF placed on a three-axis stage, we fine tune the alignment by optimizing the coupling efficiency of each individual fiber core. This is done iteratively by shifting the center positions and adjusting the divergence of the beamlet array by tuning the phase patterns on the SLM. Typically, after two iterations, a coupling efficiency of 80 % can be obtained. This step is crucial since any light not coupled into the single mode cores remain guided in the inner cladding and ends up transported to the distal end. However, most of it ends up as an incoherent background and does not contribute to the interferometric focusing process due to the temporal walk-off between the modes in the multi-mode inner cladding.

A telescope (M = 20, NA = 0.45) images the distal end of the MCF onto a CMOS camera (BlackFly S, FLIR). This calibration system (Fig. 2, red outline) serves the purpose of both measuring the transmission matrix of the fiber and to quantify several metrics such as the focusing efficiency, the lateral and axial point function in the linear regime after the phase compensation. For the two-photon imaging experiments, the detection system (Fig. 2, green outline) is fully placed behind the proximal end of the fiber. It consists of the epi-detection through the same objective (Nikon, NA = 0.75), spectrally filtered (band-pass and laser line filter) and the resulting two-photon excited fluorescence (TPEF) signal is focused on to a single pixel photo-

multiplier tube (PMT, Hamamatsu). Hence, this epi-detection geometry is fully compatible with an endoscopic configuration with no access to the distal end of the fiber during the imaging experiments.

The inter-core group delay dispersion of the MCF samples was measured by the method of Ref. [25] and a standard deviation of 71 fs was found, which is lower than the 150 fs duration of the employed laser.

We now compare the PSF of the MCF samples. After the measurement of the transmission matrix in both the cases, we generate a focal spot at the center of the field-of-view. A representative PSF is shown in Fig. 3(a). We compared the ability to scan the focus across the field-of-view using the memory effect ie the effect by which an additional phase ramp on the SLM phase mask causes a transverse shift of the PSF proportional to the slope of the ramp. Figure 3(b) depicts the field-of-view measured as the full-width at half maximum of the PSF intensity as a function of transverse position—when using the memory effect to displace the focus. We see that in the case of Fiber A, it is fully preserved, as the curve corresponds to the diameter of the mode field emitted from one core propagated to the same plane. Or in other words the field-of-view is diffraction limited. As for Fiber B, the field-of-view is diminished by about half. In the latter case point-scanning cannot be realized solely by phase ramps and would require a TM based update of the phase pattern on the SLM. Hence, despite its better Strehl ratio, Fiber B would require a high speed SLM to perform fast imaging. In the case of Fiber A, once the initial calibration is performed, the scanning operation can be fully performed with a conventional scanner and will be compatible with high speed imaging [18].

We measured the Strehl ratio and the PSF diameter as a function of the distance from the fiber end face for both MCF samples. The results are depicted in Fig. 4. We measure the Strehl ratio in the far-field to be 10 % for Fiber A and 20 % for Fiber B indicating a significant improvement from the untapered MCF (2–3 %). We see that the resulting Strehl ratio and the PSF diameter are higher for Fiber B at all working distances. The Strehl ratio for Fiber A is in line with expectations, 10 %. A discrepancy persists for Fiber B : 20 % vs. 34 %. This discrepancy is likely due to a cumulation of imperfections like residual birefringence of the cores and residual inter-core group delay dispersion [13]. The PSF diameter is systematically larger in Fiber B than in Fiber A. In the far-field, this can be understood as a consequence of the different diameters—Fiber B with its distal diameter 0.67 times that of Fiber A the divergence angle of the 0'th order will be 1/0.67 that of Fiber A.

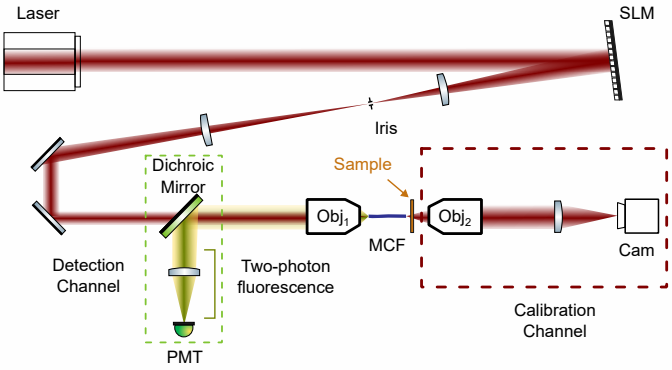

Fig. 2. Experimental setup including both the calibration and the endoscopic detection channels

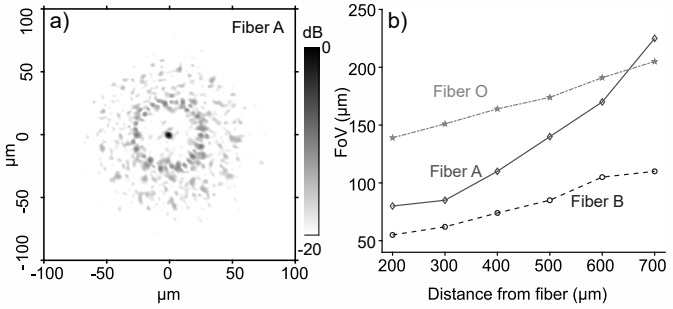

Fig. 3. Experimental characterization. (a) A representative point spread function (linear) at a distance 300 μm from the end-face for fiber A. (b) Measured field-of-view for fibers O, A, and B as a function of working distance from the MCF distal end face.

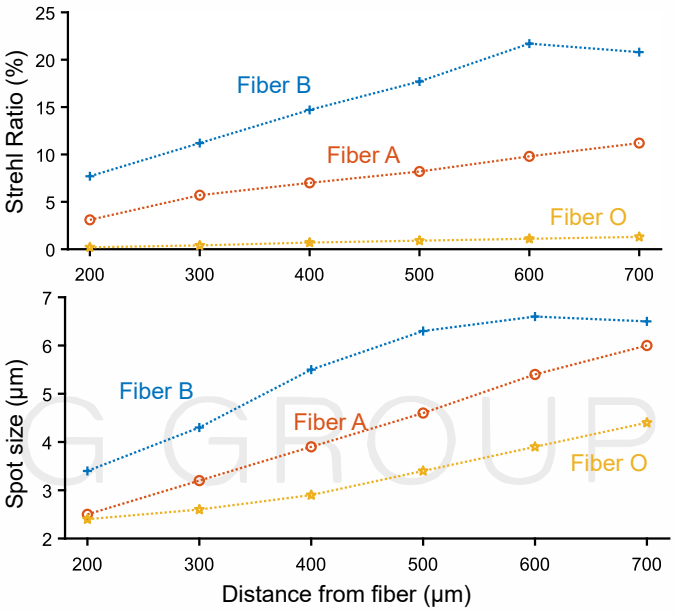

Fig. 4. Experimental characterization of the Strehl ratio and the PSF diameters for Fibers O, A, B at various distances from the fiber end face.

We demonstrate the feasibility of two-photon fluorescence imaging of biological samples in a fully endoscopic configuration with Fiber A. After an initial calibration to generate a focused beam at the center of the field-of-view, all the imaging experiments are performed with no access to the distal end. In order to ease the experimental implementation, we impose phase tilts using the SLM, and this limits the pixel-dwell time to about 100 ms. However as indicated in the earlier section, this operation could be performed with faster scanners.

We highlight the results on two different types of biological samples. First, mammalian osteosarcoma cells whose actin network has been labeled with the fluorescent marker ATTO-488 [Fig. 5(a) and Fig. 5(b)]. These filaments are well below the resolution limit of our endoscope, nevertheless the actin bundles are highlighted due to the TPEF imaging contrast. Finally, we demonstrate the imaging of GFP-labeled neurons in a 100 μm thick slice from mouse hippocampus [Fig. 5(c)]. This is a far more challenging sample for multiple reasons as it is highly scattering, densely labeled, a non-negligible background fluo-

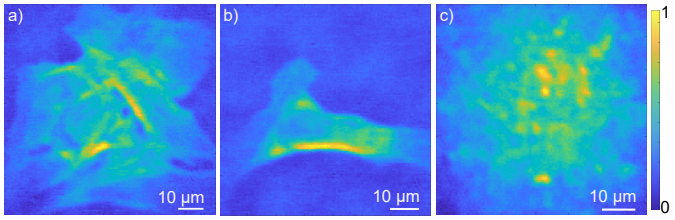

Fig. 5. Two-photon fluorescence imaging with Fiber A. (a) and (b) Mammalian osteosarcoma cells labeled with ATTO-488 and (c) GFP-labeled neurons in a 100 μm thick slice of the hippocampus of a mouse.

rescence and the relatively dimmer dye (GFP). These imaging demonstrations highlight the improved efficiency of the focusing process with the tapered fibers and the high-sensitivity of the double-clad collection.

We compared the two-photon signal levels in the two-photon lensless endoscope images of osteocarcoma cells to that obtained in a conventional two-photon microscope. We find roughly a factor 190 higher two-photon flux with the microscope. Considering the acquisition parameters ((Endoscope) λ = 925 nm ; τ = 180 fs ; f_{rep} = 80 MHz ; P_{ave} = 60 mW ; $\Delta t_{\mathrm{dwell}}$ = 100 ms ; NA = 0.22 (excitation) ; NA = 0.48 (collection) ; 30×30 pixels. (Microscope) λ = 925 nm ; τ = 180 fs ; f_{rep} = 80 MHz ; P_{ave} = 50 mW ; $\Delta t_{\mathrm{dwell}}$ = 70 μs ; NA = 1.1 ; 250×250 pixels.) the expected factor is around 27, reasonably close to the observation. The two-photon flux will always be lower in the lensless endoscope configuration, due to the inherent limits on NA posed by the MCF. Some of the difference can be absorbed by increased pixel dwell time and reduced pixel count as the field-of-view is inherently smaller due, again to the dimensions of the MCF.

In this letter, we have demonstrated two major improvements over the state of the art in two-photon lensless endoscopes as reported in Ref. 13—a diffraction-limited field-of-view and high collection efficiency (NA = 0.48), in addition to around a factor five increase in PSF intensity. This was achieved by fabricating a novel MCF with a Fermat's golden spiral core layout and post-processing steps that include tapering and re-coating the fibers with a low-index polymer inner cladding. We identify the optimal tapering ratio that delivers significant power in to the focus (10 %) and still remains compatible with high-speed scanning with a conventional scanner. Finally, we demonstrated the imaging of biological samples in an endoscopic configuration with the improved fibers. This opens up the possibility of high-speed imaging of biological samples with a lensless endoscope.

Funding. Agence Nationale de la Recherche (ANR-20-CE19-0028) Agence Nationale de la Recherche (ANR-23-CE24-0003) Agence Nationale de la Recherche (ANR-11-IDEX-0001-02, ANR-21-ESRS-0002 IDEC, ANR-21-ESRE-0003 CIRCUITPHOTONICS); INSERM (18CP128-00, PC201508); Centre National de la Recherche Scientifique, Aix-Marseille Université (A-M-AAP-ID-17-13-170228-15.22-RIGNEAULT); National Institute of Health (NIH R21 EY029406-01).

Acknowledgment. Parts of this work were developed at IRCICA (USR CNRS 3380, https://ircica.univ- lille.fr/) using FiberTech Lille facilities (https://fibertech.univ-lille.fr/en/). This work was carried out within the framework of the Contrat de Plan Etat-Region (CPER) WaveTech@HdF, supported by Ministry of Higher Education and Research, Région Hauts-de-France (HdF), Lille Metropole (MEL) and CNRS Physique.

Disclosures. The authors declare no conflicts of interest.

Data availability. Data underlying the results presented in this paper are not publicly available at this time but may be obtained from the authors upon reasonable request.

REFERENCES

1. S. Turtaev, I. T. Leite, T. Altwegg-Boussac, et al., Light Sci. Appl. **7**, 92 (2018).
2. S. Ohayon, A. Caravaca-Aguirre, R. Piestun, and J. J. DiCarlo, Biomed. Opt. Express **9**, 1492 (2018).
3. S. A. Vasquez-Lopez, R. Turcotte, V. Koren, et al., Light Sci. Appl. **7**, 110 (2018).
4. Y. Choi, C. Yoon, M. Kim, et al., Phys. review letters **109**, 203901 (2012).
5. M. Plöschner, T. Tyc, and T. Čižmár, Nat. Photonics **9**, 529 (2015).
6. A. J. Thompson, C. Paterson, M. A. A. Neil, et al., Opt. Lett. **36**, 1707 (2011).
7. Y. Kim, S. C. Warren, J. M. Stone, et al., IEEE J. Sel. Top. Quantum Electron. **22**, 171 (2016).
8. D. B. Conkey, N. Stasio, E. E. Morales-Delgado, et al., J. Biomed. Opt. **21**, 045002 (2016).
9. S. C. Warren, Y. Kim, J. M. Stone, et al., Opt. Express **24**, 21474 (2016).
10. R. Kuschmierz, E. Scharf, D. F. Ortegón-González, et al., Light. Adv. Manuf. **2**, 1 (2021).
11. S. Guérit, S. Sivankutty, J. Lee, et al., SIAM J. on Imaging Sci. **15**, 387 (2022).
12. E. Andresen, S. Sivankutty, V. Tsvirkun, et al., J. Biomed. Opt. **21**, 121506 (2016).
13. F. El Moussawi, M. Hofer, D. Labat, et al., ACS Photonics **9**, 2547 (2022).
14. E. Andresen, S. Sivankutty, G. Bouwmans, et al., J. Opt. Soc. Am. B: Opt. Phys. **32**, 1221 (2015).
15. V. Tsvirkun, S. Sivankutty, G. Bouwmans, et al., Opt. Express **25**, 31863 (2017).
16. V. Tsvirkun, S. Sivankutty, K. Baudelle, et al., Optica **6**, 1185 (2019).
17. I. Freund, M. Rosenbluh, and S. Feng, Phys. review letters **61**, 2328 (1988).
18. E. R. Andresen, G. Bouwmans, S. Monneret, and H. Rigneault, Opt. Lett. **38**, 609 (2013).
19. S. Sivankutty, A. Bertoncini, V. Tsvirkun, et al., Opt. Lett. **46**, 4968 (2021).
20. L. Wang, P. Lei, X. Wen, et al., Opt. Express **27**, 1282 (2019).
21. M. Bianco, A. Balena, M. Pisanello, et al., Biomed. Opt. Express **12**, 993 (2021).
22. J. Roper, "Advances in multicore optical fibres for endoscopy," Ph.D. thesis, University of Bath (2015).
23. R. Bernard, A. Pastre, and L. Lago-Rached, "COATING A FIBRE, PARTICULARLY AN OPTICAL FIBRE, WITH A BORON NITRIDE-BASED COATING," FR patent application 2207160 (12 July 2022).
24. D. Septier, D. Labat, A. Pastre, et al., J. Light. Technol. **41**, 4792 (2023).
25. E. R. Andresen, S. Sivankutty, G. Bouwmans, et al., J. Opt. Soc. Am. B **32**, 1221 (2015).

FULL REFERENCES

1. S. Turtaev, I. T. Leite, T. Altwegg-Boussac, et al., "High-fidelity multimode fibre-based endoscope for deep brain in vivo imaging," Light Sci. Appl. **7**, 92 (2018).
2. S. Ohayon, A. Caravaca-Aguirre, R. Piestun, and J. J. DiCarlo, "Minimally invasive multimode optical fiber microendoscope for deep brain fluorescence imaging," Biomed. Opt. Express **9**, 1492–1509 (2018).
3. S. A. Vasquez-Lopez, R. Turcotte, V. Koren, et al., "Subcellular spatial resolution achieved for deep-brain imaging in vivo using a minimally invasive multimode fiber," Light Sci. Appl. **7**, 110 (2018).
4. Y. Choi, C. Yoon, M. Kim, et al., "Scanner-free and wide-field endoscopic imaging by using a single multimode optical fiber," Phys. review letters **109**, 203901 (2012).
5. M. Plöschner, T. Tyc, and T. Čižmár, "Seeing through chaos in multimode fibres," Nat. Photonics **9**, 529–535 (2015).
6. A. J. Thompson, C. Paterson, M. A. A. Neil, et al., "Adaptive phase compensation for ultracompact laser scanning endomicroscopy," Opt. Lett. **36**, 1707 (2011).
7. Y. Kim, S. C. Warren, J. M. Stone, et al., "Adaptive Multiphoton Endomicroscope Incorporating a Polarization-Maintaining Multicore Optical Fibre," IEEE J. Sel. Top. Quantum Electron. **22**, 171–178 (2016).
8. D. B. Conkey, N. Stasio, E. E. Morales-Delgado, et al., "Lensless two-photon imaging through a multicore fiber with coherence-gated digital phase conjugation," J. Biomed. Opt. **21**, 045002 (2016).
9. S. C. Warren, Y. Kim, J. M. Stone, et al., "Adaptive multiphoton endomicroscopy through a dynamically deformed multicore optical fiber using proximal detection," Opt. Express **24**, 21474 (2016).
10. R. Kuschmierz, E. Scharf, D. F. Ortegón-González, et al., "Ultra-thin 3D lensless fiber endoscopy using diffractive optical elements and deep neural networks," Light. Adv. Manuf. **2**, 1 (2021).
11. S. Guérit, S. Sivankutty, J. Lee, et al., "Compressive Imaging Through Optical Fiber with Partial Speckle Scanning," SIAM J. on Imaging Sci. **15**, 387–423 (2022).
12. E. Andresen, S. Sivankutty, V. Tsvirkun, et al., "Ultrathin endoscopes based on multicore fibers and adaptive optics: A status review and perspectives," J. Biomed. Opt. **21**, 121506 (2016).
13. F. El Moussawi, M. Hofer, D. Labat, et al., "Tapered Multicore Fiber for Lensless Endoscopes," ACS Photonics **9**, 2547–2554 (2022).
14. E. Andresen, S. Sivankutty, G. Bouwmans, et al., "Measurement and compensation of residual group delay in a multi-core fiber for lensless endoscopy," J. Opt. Soc. Am. B: Opt. Phys. **32**, 1221–1228 (2015).
15. V. Tsvirkun, S. Sivankutty, G. Bouwmans, et al., "Bending-induced inter-core group delays in multicore fibers," Opt. Express **25**, 31863–31875 (2017).
16. V. Tsvirkun, S. Sivankutty, K. Baudelle, et al., "Flexible lensless endoscope with a conformationally invariant multi-core fiber," Optica **6**, 1185–1189 (2019).
17. I. Freund, M. Rosenbluh, and S. Feng, "Memory effects in propagation of optical waves through disordered media," Phys. review letters **61**, 2328 (1988).
18. E. R. Andresen, G. Bouwmans, S. Monneret, and H. Rigneault, "Toward endoscopes with no distal optics: video-rate scanning microscopy through a fiber bundle," Opt. Lett. **38**, 609–611 (2013).
19. S. Sivankutty, A. Bertoncini, V. Tsvirkun, et al., "Miniature 120-beam coherent combiner with 3D-printed optics for multicore fiber-based endoscopy," Opt. Lett. **46**, 4968 (2021).
20. L. Wang, P. Lei, X. Wen, et al., "Tapered fiber-based intravascular photoacoustic endoscopy for high-resolution and deep-penetration imaging of lipid-rich plaque," Opt. Express **27**, 1282–12840 (2019).
21. M. Bianco, A. Balena, M. Pisanello, et al., "Comparative study of autofluorescence in flat and tapered optical fibers towards application in depth-resolved fluorescence lifetime photometry in brain tissue," Biomed. Opt. Express **12**, 993–1009 (2021).
22. J. Roper, "Advances in multicore optical fibres for endoscopy," Ph.D. thesis, University of Bath (2015).
23. R. Bernard, A. Pastre, and L. Lago-Rached, "COATING A FIBRE, PARTICULARLY AN OPTICAL FIBRE, WITH A BORON NITRIDE-BASED COATING," FR patent application 2207160 (12 July 2022).
24. D. Septier, D. Labat, A. Pastre, et al., "Hollow core double-clad fiber coupler for nonlinear micro-endoscopy," J. Light. Technol. **41**, 4792–4798 (2023).
25. E. R. Andresen, S. Sivankutty, G. Bouwmans, et al., "Measurement and compensation of residual group delay in a multi-core fiber for lensless endoscopy," J. Opt. Soc. Am. B **32**, 1221–1228 (2015).